GEOCHEMISTRY

Archean cratonic mantle recycled at a mid-ocean ridge

Chuan-Zhou Liu[1,2,3,4]*, Henry J.B. Dick[5], Ross N. Mitchell[1], Wu Wei[1,4], Zhen-Yu Zhang[1,4], Albrecht W. Hofmann[6], Jian-Feng Yang[1], Yang Li[1]

Basalts and mantle peridotites of mid-ocean ridges are thought to sample Earth's upper mantle. Osmium isotopes of abyssal peridotites uniquely preserve melt extraction events throughout Earth history, but existing records only indicate ages up to ~2 billion years (Ga) ago. Thus, the memory of the suspected large volumes of mantle lithosphere that existed in Archean time (>2.5 Ga) has apparently been lost somehow. We report abyssal peridotites with melt-depletion ages up to 2.8 Ga, documented by extremely unradiogenic $^{187}Os/^{188}Os$ ratios (to as low as 0.1095) and refractory major elements that compositionally resemble the deep keels of Archean cratons. These oceanic rocks were thus derived from the once-extensive Archean continental keels that have been dislodged and recycled back into the mantle, the feasibility of which we confirm with numerical modeling. This unexpected connection between young oceanic and ancient continental lithosphere indicates an underappreciated degree of compositional recycling over time.

INTRODUCTION

The asthenosphere, a mechanically weak layer below the drifting rigid lithospheric plates, is important for mantle convection and crust formation on Earth. Although the asthenosphere has been widely thought to be well homogenized by mantle convection (*1*), there is now abundant evidence that it is highly heterogeneous in composition, containing widely distributed, severely melt-depleted mantle domains (*2*–*5*). Nevertheless, such ultradepleted geochemical signatures are only rarely detected in mid-ocean ridge basalts (MORBs) (*6*) and ocean island basalts (*7*). This is likely because an ultradepleted mantle is highly refractory due to ancient melt extraction (*5*), and it can produce only very small volumes of magma that are masked by the large volume of normal MORB generated in the melting column. Ancient ultradepleted signals are therefore best preserved in residual abyssal peridotites, where their depletion ages can be recognized by Os isotopes (*8*) and Hf isotopes (*9*). Abyssal peridotites with Paleoproterozoic Os model ages as old as 2.2 billion years (Ga) have been found (*3*, *5*), but the origin of such ancient mantle domains remains controversial. They could be an ancient oceanic lithospheric mantle recycled through subduction (*5*), or they might be fragments of a refractory subcontinental lithospheric mantle (SCLM) (*10*). Disruption of the SCLM beneath Archean cratons is not uncommon (*11*, *12*), and ancient lithospheric material is therefore expected to exist in the asthenosphere. However, abyssal peridotites with Archean depletion ages (>2.5 Ga) have been absent from the published record. Moreover, if disrupted SCLM can be transported by the asthenosphere to mid-ocean ridges forming new oceanic lithosphere that is ultimately subducted, the existence of ancient SCLM in the convecting mantle at large may be greatly underestimated at present.

The ultraslow-spreading Southwest Indian Ridge (SWIR), with a near-constant full spreading rate of ~14 mm year^{-1}, is an ideal place to test for the potential existence of Archean mantle at a mid-ocean ridge. It is located at a distance of ~2000 km from the nearest Archean craton, Kaapvaal, in South Africa (Fig. 1A). The SWIR spans 7700 km between the Bouvet and Rodriguez triple junctions with an overall unusually steep trend (~60°) to the spreading direction relative to the ridge axis. It generally has a crustal thickness of ~2 to 6 km, with large, widely spaced volcanic edifices and intervening regions where the mantle is exposed directly on the seafloor (*13*). Named for the cruises on which the samples were dredged, the Knorr and Protea peridotites were sampled west and east of the Andrew Bain fracture zone (FZ), respectively (Fig. 1, B and C). Details of the locations, petrography, and major element geochemistry of the studied samples are provided in Materials and Methods.

RESULTS

Major and trace elements

The studied SWIR abyssal peridotites with protogranular to porphyroclastic textures have variable compositions (table S1). They are all partially serpentinized and weathered, with variable values of loss on ignition (LOI) up to 13 weight % (wt %). A few Protea samples are quite fresh, with LOI values of <2 wt %. The Knorr samples overall have higher SiO_2 contents than the Protea samples (fig. S2). The Protea samples have relatively fertile compositions with 1.04 to 3.33 wt % Al_2O_3 (Fig. 2A), similar to abyssal peridotites globally (*14*). The Knorr samples have more variable Al_2O_3 contents of 0.34 to 2.59 wt % and can be subdivided into high- and low-Fo groups (data S2) according to olivine forsterite [Fo; 100 × Mg/(Mg + Fe)] contents. The low-Fo Knorr group has relatively fertile compositions (i.e., with Al_2O_3 contents of >1 wt %) similar to the Protea samples, whereas the high-Fo Knorr (HFK) samples are more refractory, with mostly Al_2O_3 contents of <1 wt %. While both the Protea and low-Fo Knorr peridotites have olivine Fo of <91.5, the HFK peridotites have Fo of >91.5 (Fig. 2B); the latter also have higher spinel Cr# [Cr/(Cr + Al)] values than the former (fig. S2). Compared to orthopyroxene (Opx) in the Protea and low-Fo Knorr peridotites, Opx in the HFK samples have higher Mg# [Mg/(Mg + Fe)] but lower Al_2O_3 contents (fig. S3, A and B). Overall, the HFK samples are the most refractory peridotites ever recorded from the seafloor.

[1]State Key Laboratory of Lithospheric Evolution, Institute of Geology and Geophysics, Chinese Academy of Sciences, Beijing 100029, China. [2]Laboratory for Marine Geology, Qingdao National Laboratory for Marine Science and Technology, Qingdao 266061, China. [3]CAS Center for Excellence in Deep Earth Sciences, Guangzhou 510640, China. [4]University of Chinese Academy of Sciences, Beijing 100049, China. [5]Department of Geology and Geophysics, Woods Hole Oceanographic Institution, Woods Hole, MA 02543, USA. [6]Max-Planck Institut für Chemie, Mainz 55128, Germany. *Corresponding author. Email: chzliu@mail.iggcas.ac.cn

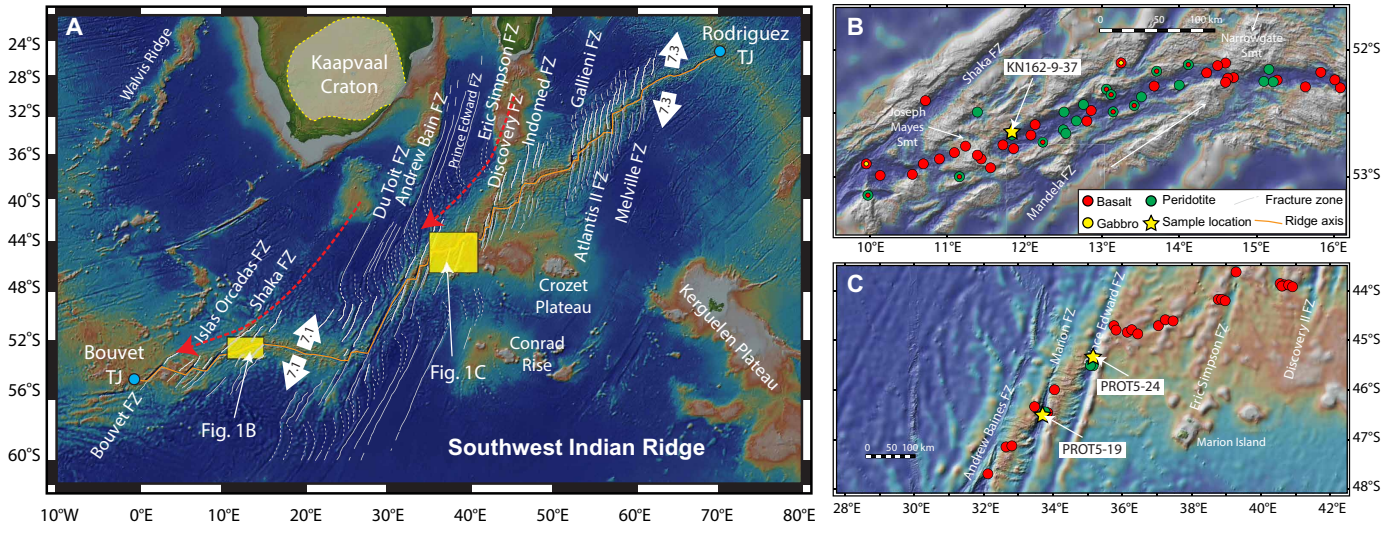

Fig. 1. Map of the SWIR and sample locations. (**A**) Spreading directions and half rates are given in millimeters on the arrows. The red dashed arrows are the mantle flow field constrained by seismic anisotropy (*36*). (**B**) The super oblique segment of the SWIR (9° E to 16°E). The dredge haul KN162-9-37, from which both high-Fo and low-Fo peridotites were sampled, is located to the right of the largest non–hot spot volcano, Joseph Mayes Seamount. (**C**) The central segment of the SWIR (28°E to 42°E), where dredge hauls PROT5-19 and PROT5-24 are located. Other dredged samples shown are from the PetDB database (www.earthchem.org/petdb). TJ, triple junction.

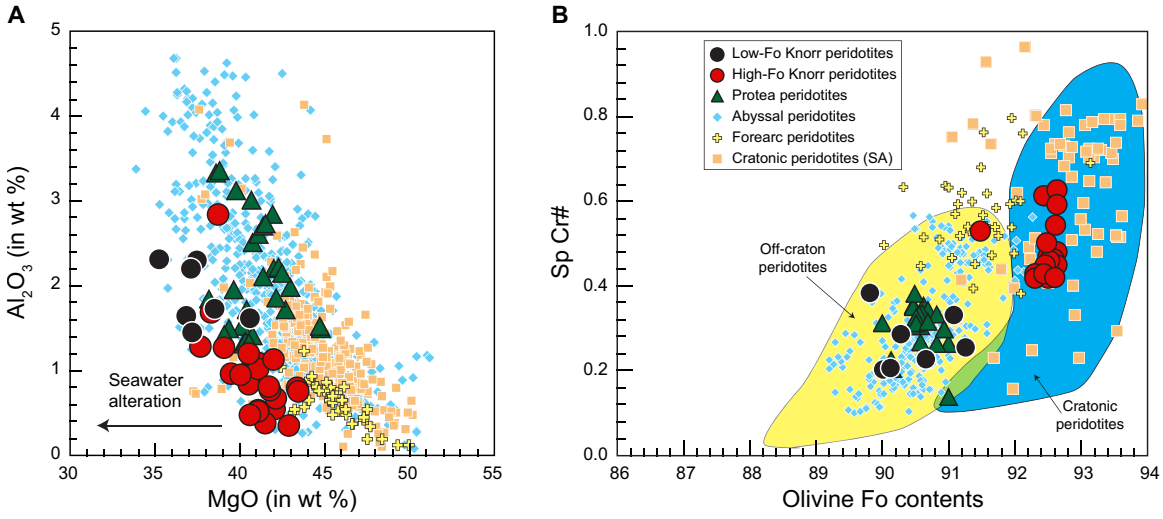

Fig. 2. Geochemistry of SWIR abyssal peridotites. (**A**) Whole-rock MgO versus Al_2O_3. (**B**) Olivine Fo contents versus spinel Cr# values. Fields of cratonic and off-craton peridotites are from (*56*). Data sources of abyssal peridotites, forearc peridotites, and South African (SA) cratonic peridotites are from the PetDB database (www.earthchem.org/petdb).

Both the Protea and low-Fo Knorr samples are relatively fertile; their low olivine Fo contents and spinel Cr# indicate a relatively low degree of partial melting. Using the function [$F = 10 \times \ln(\text{Cr\#}) + 24$] between spinel Cr# values and melting starting from a least-depleted abyssal peridotite (*15*), the Protea samples have experienced a minimum of 4 to 14% degrees of fractional melting, and the low-Fo Knorr samples have experienced 8 to 14% (table S2). Similar extents are also inferred from the heavy rare earth element (HREE) contents of their clinopyroxene (Cpx) (fig. S4 and table S3). The relatively fertile compositions of these samples, based on spinel Cr#, are not distinguishable from those of global abyssal peridotites (fig. S2). By contrast, the HFK samples are more refractory with much higher spinel Cr# values (0.42 to 0.63) and olivine Fo contents (91.5 to 92.6); their Opx and Cpx both have higher Mg# values (table S2), and their estimated degree of fractional melting is a minimum of 15 to 20%. Such high extents of melting are also indicated by remarkably lower Ti and HREE contents in their Opx than those of both the Protea and low-Fo Knorr peridotites (fig. S5 and table S3). Cpx large enough for laser ablation analysis was absent in almost all HFK peridotites except KN162-9-37-66, which is more enriched in light rare earth elements (LREEs) relative to HREE (fig. S4), with a $(Ce/Yb)_N$ [chondrite-normalized according to (*16*)] ratio of ~8. Such a LREE-enriched pattern is atypical of abyssal peridotites (*14*) but common in metasomatized cratonic mantle xenoliths (*17*).

Highly siderophile elements and Re-Os isotopes

Both highly siderophile element (HSE; including Os, Ir, Ru, Pt, Pd, and Re) contents and Re-Os isotopes are listed in table S4. The Protea and low-Fo Knorr samples have relatively flat HSE patterns (fig. S6A) similar to global abyssal peridotites (*8*, *18*), whereas the HFK samples are strongly depleted in Pd (fig. S6B). Most HFK samples have Pd/Ir ratios remarkably lower than abyssal peridotites globally (fig. S7) but similar to cratonic mantle xenoliths that underwent high extents of melting (*19*). The Protea samples have highly variable Re contents [i.e., 0.07 to 1.42 parts per billion (ppb)], with some higher than the inferred value of the primitive upper mantle [PUM; (*20*); 0.35 ± 0.06 ppb]. Their $^{187}Os/^{188}Os$ ratios range from 0.1163 to 0.13054, yielding Re depletion ages (T_{RD}) relative to PUM younger than 1.89 Ga. The low-Fo Knorr samples have relatively radiogenic $^{187}Os/^{188}Os$ ratios of 0.12288 to 0.13849; most have $^{187}Os/^{188}Os$ ratios higher than the PUM, possibly due to seafloor weathering (*21*) or melt refertilization (*22*), and cannot yield meaningful Os model ages. Two of them, with $^{187}Os/^{188}Os$ ratios lower than PUM, yield T_{RD} ages younger than 1 Ga. Similarly, young T_{RD} ages (0.23 to 0.69 Ga) have been reported for five peridotites from the same oblique ridge segment (*8*). In comparison, all HFK peridotites except three (KN162-9-37-46, -63, and -84) have very unradiogenic $^{187}Os/^{188}Os$ ratios of 0.1095 to 0.11323, which yield much older T_{RD} ages, varying from Paleoproterozoic to Neoarchean (2.28 to 2.78 Ga). The HSE patterns of the Knorr samples also indicate the late addition of Re (fig. S6B), resulting in their variable Re contents. Nevertheless, the Knorr peridotites, particularly the HFK peridotites, have low $^{187}Re/^{188}Os$ ratios (commonly <0.1), which have negligible effects on their $^{187}Os/^{188}Os$ ratios. Neither the Knorr nor the Protea samples exhibit a correlation between whole-rock Al_2O_3 and $^{187}Os/^{188}Os$ ratios (fig. S8).

DISCUSSION

Overall, the HFK peridotites have highly refractory compositions that are different from most abyssal peridotites. They have high olivine Fo and spinel Cr#; in particular, two samples (KN162-9-37-15 and -28) have spinel Cr# values higher than 0.6, which are exceedingly rare in residual abyssal peridotites (*14*). High-Cr# spinel occurs both in forearc peridotites that experienced hydrous melting (*23*) and in Archean cratonic mantle xenoliths that have experienced very high degrees of melting (*17*). The HFK samples have olivine grains (Fo of >91.5) that are more magnesian than those in forearc peridotites (*23*, *24*), plotting within the cratonic mantle xenolith field (Fig. 2B). It should be noted that the HFK peridotites have relatively higher whole-rock SiO_2 contents than the low-Fo Knorr and Protea peridotites (fig. S1), which might reflect the Si-metasomatism, a phenomenon that has been previously described for the Archean cratonic mantle xenoliths (*25*).

The Re-Os isotope system is the best tool to constrain the timing of melt extraction experienced by mantle peridotites, and the rhenium depletion age (T_{RD}) provides the minimum estimate of their ages (see Materials and Methods). The Protea peridotites show a histogram of $^{187}Os/^{188}Os$ ratios very similar to abyssal peridotites globally (Fig. 3), with T_{RD} ages younger than 1.9 Ga; similarly, old Os model ages have been reported for abyssal peridotites from the Mid-Atlantic Ridge (*2*, *3*) and the Arctic Gakkel Ridge (*5*). In contrast, the Knorr peridotites show a histogram of $^{187}Os/^{188}Os$ ratios similar to mantle xenoliths from South African cratons. While the low-Fo

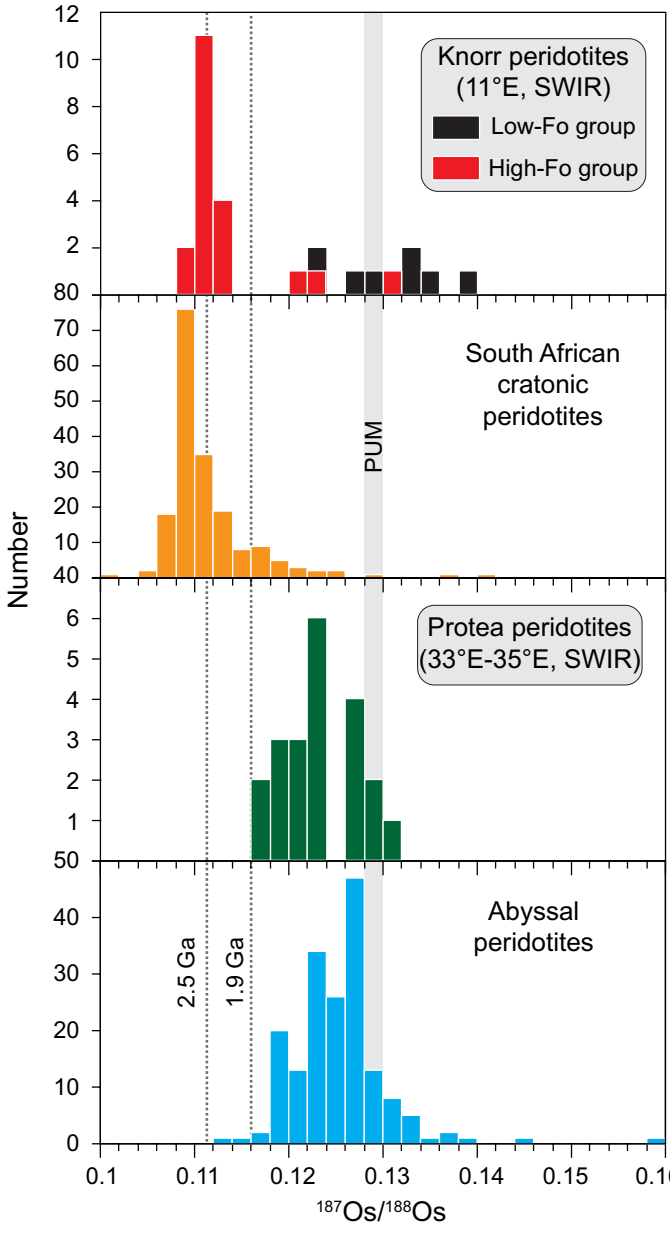

Fig. 3. Whole-rock $^{187}Os/^{188}Os$ ratios of SWIR abyssal peridotites. Two dashed lines refer to T_{RD} ages of 2.5 and 1.8 Ga, which were calculated relative to the PUM (*20*). Data of abyssal peridotites are from (*2–5*, *8*, *21*), and data of mantle xenoliths from Kaapvaal and Zimbabwe cratons are from (*19*, *57–64*). The higher $^{187}Os/^{188}Os$ ratios of SWIR peridotites than those of the PUM might be due to interaction with seawater (*21*).

Knorr peridotites also have relatively young T_{RD} ages not older than 1 Ga, the majority (17 of 20) of HFK peridotites have notably lower $^{187}Os/^{188}Os$ ratios (Fig. 3), corresponding to much older, Paleoproterozoic to Archean T_{RD} ages (2.28 to 2.78 Ga). Such Archean T_{RD} ages have not been previously reported from abyssal peridotites. Overall, most of the SWIR peridotites have been subjected to ancient partial melting events that are much older than the spreading age of the SWIR, which initiated in the Jurassic (*26*). Our results imply that the oldest model ages identified in the SWIR are dominantly Archean west of the Andrew Bain transform fault and late

Proterozoic in age to the east. Moreover, the Knorr peridotites show variable textures and model characteristics (see Materials and Methods), and therefore, they cannot have come from a single outcrop but must represent sampling consistent with the 3.6-km length of the dredge track (fig. S9). Therefore, our results substantiate the occurrence of an Archean cratonic mantle domain with a scale larger than 3 km at the western segment of SWIR.

The refractory compositions and old ages of the HFK peridotites suggest that they represent the same low-density lithologies that are found in Archean cratonic keels. The possibility that they might represent pieces of depleted Archean oceanic lithosphere, although it cannot be ruled out, is hard to be tested, as there are no preserved analogs that are actually known to be derived from Archean oceanic mantle. By contrast, samples of Archean subcontinental lithosphere are preserved as mantle xenoliths in kimberlites. As already pointed out further above, the chemical and isotopic characteristics of the HFK peridotites are notably similar to those of the cratonic lithosphere. We tested this statistically by carrying out Student's *t* test comparing the HFK samples with a population of 183 South African cratonic (SAC) peridotites and found that the two populations are indistinguishable in both Os isotopes and model ages (see Materials and Methods). For this reason, we assume that the most plausible origin of these peridotites is that they are derived from the Archean SCLM, and this will be the working hypothesis for the remainder of this paper.

This still leaves the questions of how and when these rocks were originally dislodged from the SCLM and entered the asthenosphere. The dominant mechanisms at play remain enigmatic. Loss of keels in the North China and Wyoming cratons has been attributed to subduction of the Pacific plate in the Mesozoic (*27*, *28*), in stark contrast to the tectonic setting around southern Africa that experienced no subduction in its recent geologic past. An unresolved problem encountered with the different tectonic scenarios invoked for the removal of Archean lithosphere lies in the fact that much of this

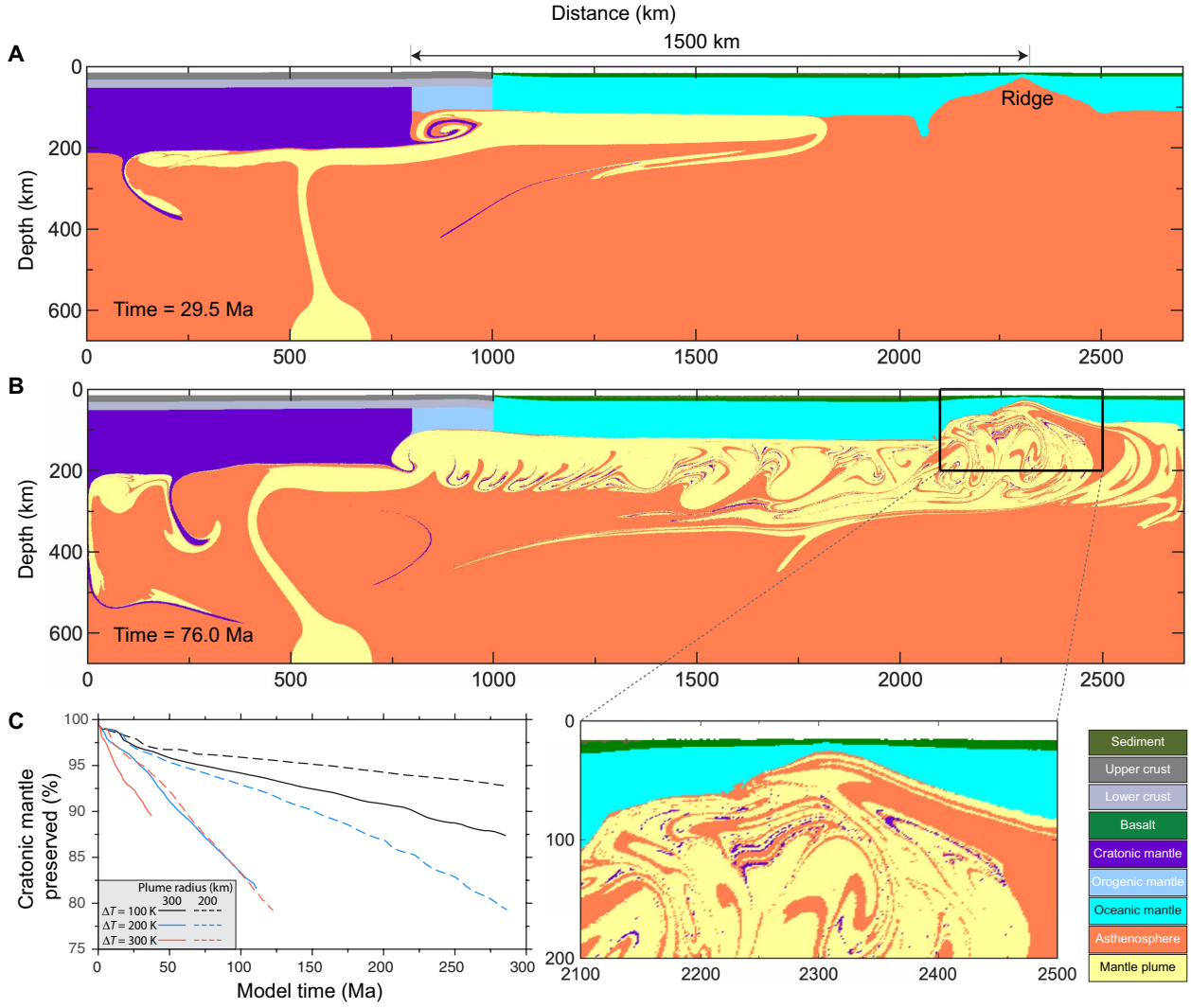

Fig. 4. Numerical modeling of proposed pathway for the recycling of Archean cratonic mantle. The dynamics of a plume entraining craton material into the asthenosphere that is then transported, due to relative buoyancy, all the way to the mid-ocean ridge. Two snapshots at 29.5 Ma (**A**) and 76 Ma (**B**) after simulation initiates. (**C**) Preserved area of cratonic mantle lithosphere during plume impingement. Model parameters used are indicated in fig. S10 in addition to exploring additional parameter space. See Fig. 5 for an artistic rendition of the mechanism, including subsequent subduction.

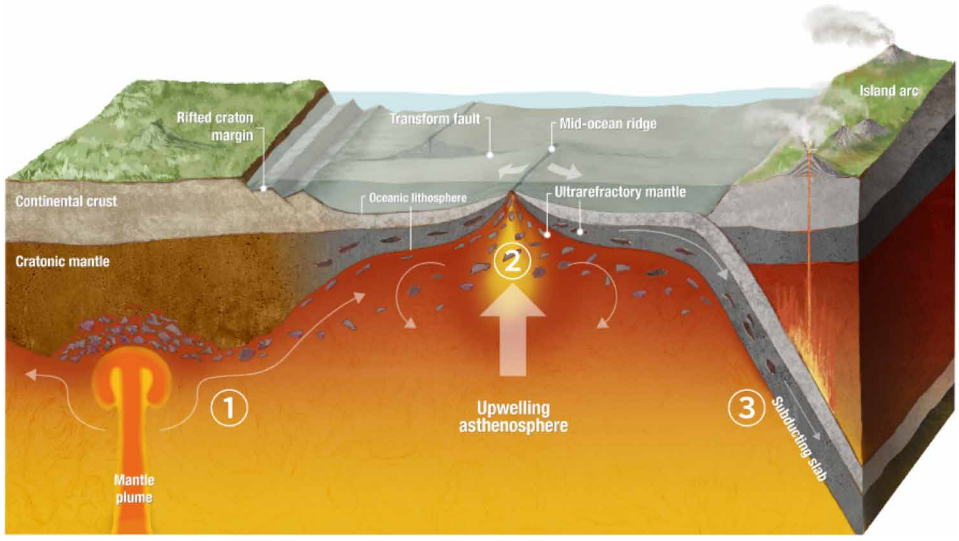

Fig. 5. Proposed pathway for the recycling of Archean cratonic mantle. (1) The cratonic mantle is disrupted by rifting and/or a mantle plume and is fragmented into the asthenosphere, after which it is transported to a mid-ocean ridge. (2) The recycled cratonic mantle is incorporated into the oceanic lithospheric mantle at a mid-ocean ridge during ultraslow seafloor spreading where it can be exposed and sampled. (3) Ultimately, subduction returns the fragments of transported Archean cratonic mantle back to the convective mantle from which it was originally extracted. The artwork was designed by Shen-Wen Wang@Institute of Planets Inc.

Archean lithospheric material consists of ultrarefractory, low-density peridotites, which are buoyant relative to the asthenospheric mantle (*11*, *29*). Consequently, delamination mechanisms invoking density-driven lithospheric loss are problematic. It has been proposed that cratonic keels can increase density by metasomatic addition of mafic components that would generate sufficient garnet to increase the bulk density of the lithosphere (*30*, *31*). Such a mechanism can be ruled out in the present case, however, because the Archean HFK samples have retained their original ultrarefractory (commonly with <1% Al_2O_3; table S1) and thus low-density properties, despite traces of metasomatism from the presence of rare Cpx (fig. S4). This indicates that the cratonic mantle can be detached even when it is buoyant, thus favoring shear flow over densification as a mechanism for SCLM loss. We suggest that the most likely agent for such shear flow is a mantle plume. Similar uncertainties exist regarding the timing of lithospheric destruction. Some models of net crustal growth contend that the mass of the late Archean continental crust reached at least 70% of the present crustal mass (*32*–*34*), which, if true, would imply that large-scale destruction of Archean crust and its associated SCLM must have taken place, given its small fraction of preserved surface ages today. Therefore, one might expect to find pieces of Archean SCLM in the modern mantle sampled at many ocean ridges that contain outcrops of mantle peridotites. However, the previous record of oceanic peridotites contains no such examples of recycled Archean SCLM, perhaps indicating that mantle mixing and homogenization processes may have destroyed most or all of this evidence.

Because neither the timing nor the mechanisms of removal of the peridotites from the subcontinental lithosphere can be independently constrained, we propose a model for this process that is consistent with the regional geology and seismic tomography. We suggest that the HFK samples were dislodged from the base of the nearest craton, the Kaapvaal craton ~1500 km away, in the relatively recent geologic past. There are at least two ways for the Kaapvaal Archean cratonic mantle to have entered the asthenosphere. It could have been disrupted along this margin during the Jurassic breakup of Gondwana and then transported in the convecting asthenosphere (*10*). Alternatively, or in combination with rifting, sustained plume activity beneath the western Gondwana cratons since the Late Cretaceous could have weakened the SCLM through warming and/or metasomatism, resulting in its erosion and thinning (*30*). Plume-triggered erosion is also supported by studies of mantle xenoliths entrained in the older (>110 Ma) and younger (<100 Ma) kimberlites in the southwest Kaapvaal craton, which revealed a thinning of ~30 km in thickness of the cratonic lithosphere over the short time span separating these two eruptive events (*35*). Transporting the eroded Archean lithospheric mantle from the Kaapvaal craton to the SWIR also fits well with the current seismically inferred mantle convective flow field (Fig. 1), which appears to be dominated by a major upwelling originating in the lower mantle beneath southern Africa and radiating away from Africa along the base of the asthenosphere under the Afar plume (*36*). Seismic tomography of the mantle beneath Africa (*37*) shows one branch of the sub-African "plume tree" extending toward the Bouvet triple junction, and it might be this branch, or its precursor, the Karoo plume, which eroded the base of the Kaapvaal craton and carried the lithospheric fragments toward the spreading ridge.

We have numerically modeled SCLM delamination by simple shear flow resulting from the impingement of a mantle plume on the base of the lithosphere and recycling of the dislodged SCLM to a spreading ridge (see Fig. 4 and Materials and Methods). The dislodgement process is similar to a previous conceptual model for lithospheric detachment (*38*), although our model does not require partial melting to occur at the base of the lithosphere. The complete recycling process is capable of shearing off sheets of lithospheric material, entraining it, introducing it into the asthenosphere, and ultimately returning parts of it to a spreading ridge ~1500 km away as in our map area (Fig. 1A). The numerical modeling results (Fig. 4) thus confirm the feasibility of the recycling mechanism that we propose to explain our data (Fig. 5). Our finding that "pristine"

ancient lithospheric material appears to exist in at least one portion of the global ridge system should reopen the search for other such occurrences and encourage a reexamination of the dynamics of such a recycling process. The apparent scarcity of the survival of such material in the present-day oceanic mantle might be caused by efficient convective stirring (*4*), which may gradually eradicate the memory of such ancient processes. Alternatively, it might simply be the result of undersampling of oceanic peridotites, which have been examined for their possible "Archean memory" by relatively few studies so far (*3*–*5*, *39*).

If such cratonic recycling can occur today, it has likely occurred throughout Earth history. Considerations from a mantle perspective of net continental growth (i.e., accounting for the effects of continental recycling and reworking) suggest that most or all of the present-day continental mass is likely to have been reached by the early Archean (*32*, *34*). However, little of this ancient crust and its lithospheric keel is preserved today in Earth's surface ages. We propose that much of the cratonic mantle and the Archean crust it protects has likely been subducted into the convecting mantle after being recycled to mid-ocean ridges. Our modeling indicates that this proposed mechanism is highly efficient, removing ~20% of the SCLM adjacent to the mantle plume in ~100 million years (Ma) (Fig. 4C), where intermittently integrating such a rate of removal during repeated episodes of rifting since the early Archean would have cumulatively removed a substantial volume of cratonic mantle to account for the observed present-day deficiency. Cratonic lithosphere delamination and recycling caused by plume-induced mantle shear flow may have been a common mechanism for craton destruction in Archean time, especially if mantle plumes were the primary agent for generating widespread, hot Archean komatiites (*40*). The history of crustal growth and destruction has been widely studied by geochemical box modeling (*34*) and by examining the surviving parts of the ancient crust (*41*). We suggest that the key for understanding the destruction part of this story is most likely not preserved in the surviving crust but must be sought in the mantle.

MATERIALS AND METHODS

Materials: SWIR abyssal peridotites

The SWIR extends 7700 km between the Bouvet and Rodriguez triple junctions (Fig. 1A) and is one of the slowest spreading mid-ocean ridge with a near-constant full spreading rate of ~14 mm year^{-1}. Much of the SWIR has a very oblique (~60°) trend from the plate spreading direction, reflecting the dominance of numerous large transform offsets (*42*). The SWIR may be divided into a number of subsections based on changes in the obliquity of the ridge axis and the variation of regional axial depths. Between the Shaka FZ at 9°E and the Du Toit FZ at 25°E, with ~1000 km in length, it consists of two sharply contrasting supersegments (*42*), i.e., the orthogonal supersegment (16°E to 25°E) and the oblique segment (9°E to 16°E). The ridge in the orthogonal segment is oriented approximately perpendicularly to the spreading direction and is linked by a 150-km slightly oblique (~10°) section. The oblique supersegment begins at the 16°E discontinuity with a 500-m drop in rift valley depth. The ridge in this supersegment is highly oblique (50° to 60°) and has a mean depth of ~4000 m. Three amagmatic accretionary segments exist within the oblique supersegment (i.e., 9°30′E to 11°E, 11°35′E to 14°15′E, and 14°54′E to 15°45′E), which are connected by the Narrowgate segment and the Joseph Mayes seamount. The three amagmatic segments have an average axial depth of 4151 ± 425 m and variable rift valley widths of ~30 to 50 km (*43*), from which abundant peridotites, scattered basalts, minimal diabases, and gabbros have been recovered. The Narrowgate segment (11°45′E to 14°54′E) is a volcanically robust, orthogonal spreading segment with a ~2700-m deep and ~20-km-wide rift valley. The Joseph Mayes seamount between 11°E and 11°35′E is spreading approximately orthogonally and is perhaps the largest non–hot spot volcano on the global ridge system (*43*).

At 25°E, the SWIR is abruptly offset about 1800 km to the northeast by the four FZs Du Toit, Andrew Bain, Marion, and Prince Edward. The three subsections between these four FZs display almost constant obliquities of 25° and have an average axial depth of ~3200 m (*44*). The Andrew Bain FZ has been suggested as the transition between Indian-like and Atlantic-like mantle sources (*45*). From the Andrew Bain FZ to the Gallieni FZ, the SWIR crosses the flank of the Southern Ocean geoid high, following a subdued positive arch over the Marion swell, starting at a depth of ~4800 m at 27°E before rising abruptly to a depth of 858 m at 36°E and then down to 5150 m at 63°E. The SWIR east of the Indomed FZ was formed by propagation of the Rodriguez triple junction (RTJ) over the past 64 Ma. It has regularly spaced nontransform discontinuities, short oblique amagmatic segments, and the Atlantis II, Novara, and Melville transforms. From 61°E to the RTJ, like in the 9°E to 25°E section, the SWIR is devoid of long-lived transform and nontransform discontinuities.

Our samples come from different regions along the SWIR. One suite, dredged by RV Knorr Cruise 162-9 (Dredge 37), is from the western end of the ~190-km-long highly oblique amagmatic segment (11°38.7′E to 14°17.2′E; Fig. 1B), ~25 km from the large alkalic Joseph Mayes seamount (*43*). The obliquity of the amagmatic segment reduces the local mantle upwelling rate, resulting in conductive cooling capping the melting column at great depth limiting melting, likely accounting for the enriched volcanism to the west (*42*). Dredge 162-9 was made from 3907 to 3433 m from near the base of the northern wall of the 9°E to 16°E rift valley (fig. S9) along a 3.6-km-long track over rough terrain. The dredge recovered a diverse assemblage mainly consisting of partially serpentinized and weathered peridotites (249 kg), with minor 0.4-kg gabbro (0.4 kg), diabase (4 kg), basalt (1 kg), and volcaniclastics (1.5 kg). The peridotites show variations in petrographic textures (fig. S10) and degrees of alteration (fig. S11). Another suite was dredged ~1700 km to the east across the Andrew Bain FZ by RV Melville Protea Expedition Leg 5 from the Marion and Prince Edward FZs, respectively (Fig. 1C), i.e., PROT 5-19 (46°34′S, 33°49′E) and PROT 5-24 (45°33′S, 35°10′E).

Major and trace elements

All measurements reported here were conducted at the Institute of Geology and Geophysics, Chinese Academy of Sciences (IGGCAS). Whole-rock major elements were analyzed using x-ray fluorescence. Mineral major elements were measured by a Cameca SX Five electron microprobe, using an acceleration potential of 15 kV, a beam current of 30 nA, and a spot size of 5 μm. Trace elements of both Cpx and Opx were determined by laser ablation system, which consists of an Element XR HR-ICP-MS instrument (Thermo Fisher Scientific, USA) and a 193-nm ArF excimer Analyte G2 laser system (Teledyne CETAC Technologies, USA). The isotopes were measured using a peak-hopping mode with a beam size of 60 μm and a repetition

rate of 5 Hz. ^{29}Si was used as an internal standard. NIST SRM 612 reference glass was used for external calibration. Both BCR-2 and BIR-1 glass were used for quality control monitoring.

HSEs and Re-Os isotopes

Whole-rock Re-Os isotopes were analyzed at the IGGCAS using the isotope dilution method (*46*). About 2 g of powders, together with a ^{187}Re-^{190}Os spike and a mixed ^{191}Ir-^{99}Ru-^{194}Pt-^{105}Pd spike, was mixed in Carius tubes, which were digested with reverse aqua regia (i.e., 3 ml of 12 N HCl and 6 ml of 16 N HNO_3) at 240°C for ~72 hours in an oven. Osmium was extracted from the aqua regia solution by solvent extraction into CCl_4 and further purified by microdistillation (*47*). Other HSEs were first separated from the solution into subgroups (Re-Ru, Ir-Pt, and Pd) using a 2-ml anion exchange resin (AG-1 × 8, 100 to 200 mesh). Subsequently, the Re-Ru was further purified by a 0.25-ml anion exchange resin; the Pd and Ir-Pt were further purified by an Eichrom LN spec resin to completely remove Zr and Hf.

Osmium concentrations and isotopes were measured by negative thermal ionization mass spectrometry on a GV IsoProbe-T instrument in static mode using Faraday cups. A $Ba(OH)_2$ solution was used as an ion emitter. The measured Os isotopes were corrected for mass fractionation using the ^{192}Os/^{188}Os ratio of 3.0827. The Nier oxygen isotope composition (^{17}O/^{16}O = 0.0003708 and ^{18}O/^{16}O = 0.002045) has been used for oxide correction. The in-run precisions for Os isotopic measurements were better than 0.2% (2σ) for all the samples. The Johnson-Matthey standard of UMD was used as an external standard, yielding an ^{187}Os/^{188}Os ratio of 0.11378 ± 2 (2σ; n = 5). Concentrations of other HSE were measured on a Thermo Fisher Scientific Neptune MC-ICPMS with an electron multiplier in peak-jumping mode or using Faraday cups in static mode, depending on the measured signal intensity. In-run precisions for ^{185}Re/^{187}Re, ^{191}Ir/^{193}Ir, ^{99}Ru/^{101}Ru, ^{194}Pt/^{196}Pt, and ^{105}Pd/^{106}Pd were 0.1 to 0.3% (2σ). The Re, Ir, Ru, Pt, and Pd standards were used to correct mass fractionations. The total procedural blanks were 3 ± 1 pg for Os, 5 ± 2 pg for Re, 1 ± 0.5 pg for Ir, 10 ± 5 pg for Ru, 20 ± 10 pg for Pt, and 10 ± 5 pg for Pd (n = 10). An ^{187}Os/^{188}Os ratio of ~0.15 was obtained for the blank. The standard UB-N was used to monitor the accuracy of the analytical procedure; results are given in table S4.

Age estimate of mantle peridotites using Re-Os isotopes

Multiple methods have been proposed to use the Re-Os isotope system to determine the ages of peridotites (*22*, *48*). As for most chronometers, the isochron is expected to provide a robust age estimate. However, meaningful Re-Os isochrons have rarely been obtained for mantle peridotites, probably because of the disturbance of this system by late-stage processes after melting in mantle peridotites (e.g., melt metasomatism). Lacking reliable isochrons, two different kinds of Os model ages have been widely applied for mantle peridoites (*49*). One is the Os model age, T_{MA}, which is calculated by using the measured ^{187}Re/^{188}Os ratio of the sample to extrapolate the measured ^{187}Os/^{188}Os ratio back in time until it intersects the evolution curve of a model mantle reservoir, e.g., the chondritic upper mantle (*49*) or the PUM (*20*). However, the reliability of the T_{MA} age is often compromised by Re mobility in mantle peridotites (the same problem encountered in determining Re-Os isochrons). For this reason, the most widely used Os model age is the rhenium depletion model age, T_{RD}, which is calculated by directly comparing the measured ^{187}Os/^{188}Os ratio of the sample to the evolution curve of a model mantle reservoir (*49*). As the T_{RD} age ignores the in-growth of ^{187}Os due to Re in mantle residues after melting, it provides a minimum estimate of the true melt-depletion age. Therefore, the T_{RD} age is most applicable for strongly refractory mantle peridotites in which Re is almost completely removed during high degrees of partial melting, with little Re remaining in the mantle residues. It should be noted that T_{RD} ages calculated relative to the evolution curve of the PUM model mantle [current ^{187}Os/^{188}Os = 0.1296; (*20*)], as shown in table S4, are ~200 Ma older than those calculated relative to "chondritic" mantle [current ^{187}Os/^{188}Os = 0.127; (*49*)]; however, Archean ages are found for some Knorr samples regardless of which evolution curve is used.

Thermomechanical numerical modeling

The two-dimensional thermomechanical numerical code I2VIS based on the finite difference method with marker-in-cell technique (*50*) was used to solve the mass, momentum, and energy conservation (Eqs. 1 to 3) using the Boussinesq approximation

$$\nabla \cdot \mathbf{V} = 0 \tag{1}$$

$$-\nabla P + \nabla[\eta(\nabla \mathbf{V} + \nabla \mathbf{V}^{T})] = \rho \mathbf{g} \tag{2}$$

$$\rho C_p \frac{DT}{Dt} = \nabla \cdot (k \nabla T) + H_r + H_s + H_a \tag{3}$$

where $\mathbf{V}$ is the velocity, P is the dynamic pressure, ρ is the density, $\mathbf{g}$ is the gravity acceleration, C_p is the specific heat, T is the temperature, k is the thermal conductivity, H_r is radioactive heating, $H_s = \tau_{ij} \times \dot{\varepsilon}_{ij}$ is shear heating, and $H_a = T\alpha\rho g v_y$ is adiabatic heating. The effective viscosity is given by $\eta = (1/\eta_{disl} + 1/\eta_{diff})^{-1}$, where η_{disl} and η_{diff} are dislocation and diffusion creep viscosities, respectively.

The effective density of rocks depending on the temperature and pressure is given by

$$\rho = \rho_0(1 - \alpha(T - T_0))(1 + \beta(P - P_0)) \tag{4}$$

where ρ_0 is the density of rock at the reference temperature (T_0=273 K) and pressure (P_0=0 Pa), α is thermal expansivity, and β is compressibility.

The model domain is 2700 km by 675 km in x-y directions, which is resolved by 901 × 226 nodes and more than 7 million markers to trace physical properties (a relatively higher resolution with 3 km by 1.5 km is also tested, and invisible difference is observed; fig. S12). All boundaries are using free slip condition, and to mimic a free surface in the finite difference, we impose a 15-km-thick sticky air (10^{18} Pa·s) (*51*, *52*). The lithosphere has a linear temperature profile with 0°C at the surface and 1350°C at the bottom, while the asthenospheric mantle has an adiabatic thermal gradient of 0.5 K km^{-1}. The top and bottom boundaries are isotherm to have fixed temperatures of 0°C at the surface and 1680°C at the bottom, respectively. The side boundaries have zero heat flux.

The laboratory-derived parameters of the flow law for olivine (*53*) are listed in table S5. The initial model setup is composed of a 200-km-thick cratonic lithosphere and a 100-km-thick orogenic lithosphere, and the mid-ocean ridge is located 1000 to 2500 km away from the craton. The thermal age of the oceanic lithosphere linearly increases from 0 Ma at the ridge to 30 Ma at 200 km away,

while a half-space cooling model is used for its thermal structure. We assume that a hot mantle plume consistently sits below the craton. Its radius and excess temperature are varied in our model (fig. S13) to investigate their influences on the ability of entrained cratonic material to be transported to the far-field ridge. Because of its low thermal structure, the cratonic lithosphere has a large effective viscosity ($>10^{23}$ Pa·s) to resist persistent mantle convection. However, mantle upwelling in a strong and large plume can erode the lithosphere at the craton's edge where thermal structures are remarkably different between two terranes and edge-driven convection is pervasive (*54*). The arrival of the mantle plume to the base of the lithosphere tends to be tilted to the orogenic lithosphere side (*55*), and in consequence, the continuously fed mantle upwelling entrained the eroded or delaminated cratonic mantle to a distance of more than 1500 km to reach the ridge in only a few tens of million years to 100 Ma.

Student's *t* test

Student's *t* test was conducted to determine whether the HFK peridotites and the SAC peridotites represent similar or distinct age populations. Because there are more SAC (n = 183) than HFK (n = 20) peridotites and Student's *t* test must be conducted on two populations of equal sample size, we resampled 20 ages from the SAC peridotites 100 times. Given the skewed age distributions of both datasets (Fig. 3), the *t* test was conducted with the one-tailed distribution. Because the two sample sets are independent of each other, the two-sample *t* test (assuming equal variance) was used. The average P value of the 100 *t* tests from the 100 resamplings was calculated. Far exceeding the typical threshold of 0.05, the value of $P = 0.26$ indicates that the null hypothesis that the two age populations are the same cannot be rejected. This result is consistent with the HFK peridotites being sampled from the same age population of the SAC peridotites. If the HFK peridotites were not sampled from the SAC peridotites, their statistically identical age populations would have to be purely coincidental.

SUPPLEMENTARY MATERIALS

Supplementary material for this article is available at https://science.org/doi/10.1126/sciadv.abn6749

REFERENCES AND NOTES

1. A. Zindler, S. Hart, Chemical geodynamics. *Annu. Rev. Earth Planet. Sci.* **14**, 493–571 (1986).
2. A. D. Brandon, J. E. Snow, R. J. Walker, J. W. Morgan, T. D. Mock, ^{190}Pt–^{186}Os and ^{187}Re–^{187}Os systematics of abyssal peridotites. *Earth Planet. Sci. Lett.* **177**, 319–335 (2000).
3. J. Harvey, A. Gannoun, K. W. Burton, N. W. Rogers, O. Alard, I. J. Parkinson, Ancient melt extraction from the oceanic upper mantle revealed by Re–Os isotopes in abyssal peridotites from the Mid-Atlantic ridge. *Earth Planet. Sci. Lett.* **244**, 606–621 (2006).
4. J. C. Lassiter, B. L. Byerly, J. E. Snow, E. Hellebrand, Constraints from Os-isotope variations on the origin of Lena Trough abyssal peridotites and implications for the composition and evolution of the depleted upper mantle. *Earth Planet. Sci. Lett.* **403**, 178–187 (2014).
5. C. Z. Liu, J. E. Snow, E. Hellebrand, G. Brügmann, A. von der Handt, A. Büchl, A. W. Hofmann, Ancient, highly heterogeneous mantle beneath Gakkel ridge, Arctic Ocean. *Nature* **452**, 311–316 (2008).
6. A. V. Sobolev, N. Shimizu, Ultra-depleted primary melt included in an olivine from the Mid-Atlantic Ridge. *Nature* **363**, 151–154 (1993).
7. A. Stracke, F. Genske, J. Berndt, J. M. Koornneef, Ubiquitous ultra-depleted domains in Earth's mantle. *Nat. Geosci.* **12**, 851–855 (2019).
8. J. M. D. Day, R. J. Walker, J. M. Warren, ^{186}Os–^{187}Os and highly siderophile element abundance systematics of the mantle revealed by abyssal peridotites and Os-rich alloys. *Geochim. Cosmochim. Acta* **200**, 232–254 (2017).
9. A. Stracke, J. E. Snow, E. Hellebrand, A. von der Handt, B. Bourdon, K. Birbaum, D. Günther, Abyssal peridotite Hf isotopes identify extreme mantle depletion. *Earth Planet. Sci. Lett.* **308**, 359–368 (2011).
10. S. Y. O'Reilly, M. Zhang, W. L. Griffin, G. Begg, J. Hronsky, Ultradeep continental roots and their oceanic remnants: A solution to the geochemical "mantle reservoir" problem? *Lithos* **112**, 1043–1054 (2009).
11. D. G. Pearson, J. M. Scott, J. Liu, A. Schaeffer, L. H. Wang, J. van Hunen, K. Szilas, T. Chacko, P. B. Kelemen, Deep continental roots and cratons. *Nature* **596**, 199–210 (2021).
12. F. Y. Wu, Y. G. Xu, R. X. Zhu, G. W. Zhang, Thinning and destruction of the cratonic lithosphere: A global perspective. *Sci. China-Earth Sci.* **57**, 2878–2890 (2014).
13. H. Y. Zhou, H. J. B. Dick, Thin crust as evidence for depleted mantle supporting the Marion Rise. *Nature* **494**, 195–200 (2013).
14. J. M. Warren, Global variations in abyssal peridotite compositions. *Lithos* **248-251**, 193–219 (2016).
15. E. Hellebrand, J. E. Snow, H. J. B. Dick, A. W. Hofmann, Coupled major and trace elements as indicators of the extent of melting in mid-ocean-ridge peridotites. *Nature* **410**, 677–681 (2001).
16. E. Anders, N. Grevesse, Abundances of the elements: Meteoritic and solar. *Geochim. Cosmochim. Acta* **53**, 197–214 (1989).
17. D. G. Pearson, D. Canil, S. B. Shirey, in *Treatise on Geochemistry*, H. D. Holland, K. K. Turekian, Eds. (Elsevier, 2014), vol. 3, pp. 169–253.
18. C. Z. Liu, J. E. Snow, G. Brügmann, E. Hellebrand, A. W. Hofmann, Non-chondritic HSE budget in Earth's upper mantle evidenced by abyssal peridotites from Gakkel ridge (Arctic Ocean). *Earth Planet. Sci. Lett.* **283**, 122–132 (2009).
19. D. G. Pearson, G. J. Irvine, D. A. Ionov, F. R. Boyd, G. E. Dreibus, Re–Os isotope systematics and platinum group element fractionation during mantle melt extraction: A study of massif and xenolith peridotite suites. *Chem. Geol.* **208**, 29–59 (2004).
20. T. Meisel, R. J. Walker, A. J. Irving, J.-P. Lorand, Osmium isotopic compositions of mantle xenoliths: A global perspective. *Geochim. Cosmochim. Acta* **65**, 1311–1323 (2001).
21. J. E. Snow, L. Reisberg, Os isotopic systematics of the MORB mantle: Results from altered abyssal peridotites. *Earth Planet. Sci. Lett.* **133**, 411–421 (1995).
22. R. L. Rudnick, R. J. Walker, Interpreting ages from Re–Os isotopes in peridotites. *Lithos* **112**, 1083–1095 (2009).
23. I. J. Parkinson, J. A. Pearce, Peridotites from the Izu-Bonin-Mariana forearc (ODP leg 125): Evidence for mantle melting and melt-mantle interaction in a supra-subduction zone setting. *J. Petrol.* **39**, 1577–1618 (1998).
24. J. M. D. Day, D. B. Brown, Ancient melt-depletion in fresh to strongly serpentinized Tonga trench peridotites. *J. Petrol.* **62**, egab088 (2021).
25. F. R. Boyd, N. P. Pokhilenko, D. G. Pearson, S. A. Mertzman, N. V. Sobolev, L. W. Finger, Composition of the Siberian cratonic mantle: Evidence from Udachnaya peridotite xenoliths. *Contri. Mineral. Petrol.* **128**, 228–246 (1997).
26. A. Tuck-Martin, J. Adam, G. Eagles, New plate kinematic model and tectono-stratigraphic history of the East African and West Madagascan Margins. *Basin Res.* **30**, 1118–1140 (2018).
27. R. W. Carlson, D. G. Pearson, D. E. James, Physical, chemical, and chronological characteristics of continental mantle. *Rev. Geophys.* **43**, RG1001 (2005).
28. F. Y. Wu, J. H. Yang, Y. G. Xu, S. A. Wilde, R. J. Walker, Destruction of the North China Craton in the Mesozoic. *Annu. Rev. Earth Planet. Sci.* **47**, 173–195 (2019).
29. S. Y. O'Reilly, W. L. Griffin, Y. H. Poudjom Djomani, Are lithospheres forever? Tracking changes in subcontinental lithospheric mantle through time. *GSA Today* **11**, 4–10 (2001).
30. J. Hu, L. Liu, M. Faccenda, Q. Zhou, K. M. Fischer, S. Marshak, C. Lundstrom, Modification of the Western Gondwana craton by plume–lithosphere interaction. *Nat. Geosci.* **11**, 203–210 (2018).
31. C. T. A. Lee, P. Luffi, E. J. Chin, Building and destroying continental mantle. *Annu. Rev. Earth Planet. Sci.* **39**, 59–90 (2011).
32. R. L. Armstrong, Radiogenic isotopes: The case for crustal recycling on a near-steadystate no-continental-growth Earth. *Phil. Trans. R. Soc. Lond. A* **301**, 443–472 (1981).
33. B. Dhuime, C. J. Hawkesworth, P. A. Cawood, C. D. Storey, A change in the geodynamics of continental growth 3 billion years ago. *Science* **335**, 1334–1336 (2012).
34. M. Guo, J. Korenaga, Argon constraints on the early growth of felsic continental crust. *Sci. Adv.* **6**, eaaz6234 (2020).
35. W. L. Griffin, S. Y. O'Reilly, N. Abe, S. Aulbach, R. M. Davies, N. J. Pearson, B. J. Doyle, K. Kivi, The origin and evolution of Archean lithospheric mantle. *Precambrian Res.* **127**, 19–41 (2003).
36. M. D. Behn, C. P. Conrad, P. G. Silver, Detection of upper mantle flow associated with the African Superplume. *Earth Planet. Sci. Lett.* **224**, 259–274 (2004).
37. M. Tsekhmistrenko, K. Sigloch, K. Hosseini, G. Barruol, A tree of Indo-African mantle plumes imaged by seismic tomography. *Nat. Geosci.* **14**, 612–619 (2021).
38. S. F. Foley, Rejuvenation and erosion of the cratonic lithosphere. *Nat. Geosci.* **1**, 503–510 (2008).
39. B. M. Urann, H. J. B. Dick, R. Parnell-Turner, J. F. Casey, Recycled arc mantle recovered from the Mid-Atlantic Ridge. *Nat. Commun.* **11**, 3887 (2020).
40. I. H. Campbell, R. W. Griffiths, R. I. Hill, Melting in an Archaean mantle plume: Heads it's basalts, tails it's komatiites. *Nature* **339**, 697–699 (1989).

41. C. J. Spencer, Continuous continental growth as constrained by the sedimentary record. *Am. J. Sci.* **320**, 373–401 (2020).
42. H. J. B. Dick, J. Lin, H. Schouten, An ultraslow-spreading class of ocean ridge. *Nature* **426**, 405–412 (2003).
43. J. J. Standish, H. J. B. Dick, P. J. Michael, W. G. Melson, T. O'Hearn, MORB generation beneath the ultraslow spreading Southwest Indian Ridge (9–25°E): Major element chemistry and the importance of process versus source. *Geochem. Geophys. Geosys.* **9**, 1–39 (2008).
44. J. E. Georgen, J. Lin, H. J. B. Dick, Evidence from gravity anomalies for interactions of the Marion and Bouvet hotspots with the Southwest Indian Ridge: Effects of transform offsets. *Earth Planet. Sci. Lett.* **187**, 283–300 (2001).
45. C. M. Meyzen, J. Blichert-Toft, J. N. Ludden, E. Humler, C. Mével, F. Albarède, Isotopic portrayal of the Earth's upper mantle flow field. *Nature* **447**, 1069–1074 (2007).
46. Z.-Y. Chu, F. Y. Wu, R. J. Walker, R. L. Rudnick, L. Pitcher, I. S. Puchtel, Y. H. Yang, S. A. Wilde, Temporal evolution of the lithospheric mantle beneath the eastern north china craton. *J. Petrol.* **50**, 1857–1898 (2009).
47. J. L. Birck, M. Roy-Barman, F. Capmas, Re-Os isotopic measurements at the femtomole level in natural samples. *Geostandard. Newslett.* **21**, 19–27 (1997).
48. S. B. Shirey, R. J. Walker, The Re-Os isotope system in cosmochemistry and high-temperature geochemistry. *Annu. Rev. Earth Planet. Sci.* **26**, 423–500 (1998).
49. R. J. Walker, R. W. Carlson, S. B. Shirey, F. R. Boyd, Os, Sr, Nd, and Pb isotope systematics of southern African peridotite xenoliths: Implications for the chemical evolution of subcontinental mantle. *Geochim. Cosmochim. Acta* **53**, 1583–1595 (1989).
50. T. V. Gerya, D. A. Yuen, Characteristics-based marker-in-cell method with conservative finite-differences schemes for modeling geological flows with strongly variable transport properties. *Phys. Earth Planet. Int.* **140**, 293–318 (2003).
51. F. Crameri, H. Schmeling, G. J. Golabek, T. Duretz, R. Orendt, S. J. H. Buiter, D. A. May, B. J. P. Kaus, T. V. Gerya, P. J. Tackley, A comparison of numerical surface topography calculations in geodynamic modelling: An evaluation of the 'sticky air' method. *Geophys. J. Int.* **189**, 38–54 (2012).
52. B. J. Kaus, H. Mühlhaus, D. A. May, A stabilization algorithm for geodynamic numerical simulations with a free surface. *Phys. Earth Planet. Inter.* **181**, 12–20 (2010).
53. S. I. Karato, P. Wu, Rheology of the upper mantle: A synthesis. *Science* **260**, 771–778 (1993).
54. J. Van Wijk, J. Van Hunen, S. Goes, Small-scale convection during continental rifting: Evidence from the Rio Grande rift. *Geology* **36**, 575–578 (2008).
55. A. Koptev, E. Calais, E. Burov, S. Leroy, T. Gerya, Dual continental rift systems generated by plume–lithosphere interaction. *Nat. Geosci.* **8**, 388–392 (2015).
56. P. E. Janney, S. B. Shirey, R. W. Carlson, D. G. Pearson, D. R. Bell, A. P. le Roex, A. Ishikawa, P. H. Nixon, F. R. Boyd, Age, composition and thermal characteristics of south african off-craton mantle lithosphere: Evidence for a multi-stage history. *J. Petrol.* **51**, 1849–1890 (2010).
57. R. W. Carlson, R. O. Moore, Age of the Eastern Kaapvaal mantle: Re-Os isotope data for peridotite xenoliths from the Monastery kimberlite. *S. Afr. J. Geol* **107**, 81–90 (2004).
58. R. W. Carlson, J. B. Dawson, P. H. Nixon, in *Proceedings of the 7th International Kimberlite Conference*, J. J. Gurney, Ed. (Cape Town, 1999), pp. 99–108.
59. A. Luguet, M. Behrens, D. G. Pearson, S. König, D. Herwartz, Significance of the whole rock Re–Os ages in cryptically and modally metasomatised cratonic peridotites: Constraints from HSE–Se–Te systematics. *Geochim. Cosmochim. Acta* **164**, 441–463 (2015).
60. A. H. Menzies, R. W. Carlson, S. B. Shirey, J. J. Gurney, in *Proceedings of the 7th International Kimberlite Conference*, J. J. Gurney, Ed. (Cape Town, 1997), pp. 566–573.
61. D. G. Pearson, R. W. Carlson, S. B. Shirey, F. R. Boyd, P. H. Nixon, Stabilisation of Archaean lithospheric mantle: A Re-Os isotope study of peridotite xenoliths from the Kaapvaal craton. *Earth Planet. Sci. Lett.* **134**, 341–357 (1995).
62. N. Simon, The origin of garnet and clinopyroxene in "depleted" Kaapvaal peridotites. *Lithos* **71**, 289–322 (2003).
63. N. S. C. Simon, R. W. Carlson, D. G. Pearson, G. R. Davies, The origin and evolution of the Kaapvaal cratonic lithospheric mantle. *J. Petrol.* **48**, 589–625 (2007).
64. C. B. Smith, D. G. Pearson, G. P. Bulanova, A. D. Beard, R. W. Carlson, N. Wittig, K. Sims, L. Chimuka, E. Muchemwa, Extremely depleted lithospheric mantle and diamonds beneath the southern Zimbabwe Craton. *Lithos* **112**, 1120–1132 (2009).
65. M. F. Horan, R. J. Walker, J. W. Morgan, J. N. Grossman, A. E. Rubin, Highly siderophile elements in chondrites. *Chem. Geol.* **196**, 27–42 (2003).
66. M. Paquet, J. M. D. Day, D. B. Brown, C. L. Waters, Effective global mixing of the highly siderophile elements into Earth's mantle inferred from oceanic abyssal peridotites. *Geochim. Cosmochim. Acta* **316**, 347–362 (2022).
67. I. J. Parkinson, C. J. Hawkesworth, A. S. Cohen, Ancient mantle in a modern arc: Osmium isotopes in izu-bonin-mariana forearc peridotites. *Science* **281**, 2011–2013 (1998).

Acknowledgments: We thank Z.-Y. Chu and Y.-H. Yang for geochemical analysis. **Funding:** This study was financially supported by the National Science Fund for Distinguished Young Scholars 42025201 (to C.-Z.L.), the National Key Research and Development Project of China 2020YFA0714801 (to C.-Z.L.), the Strategic Priority Research Program of the Chinese Academy of Sciences XDA13010106 (to C.-Z.L.), the Strategic Priority Research Program of the Chinese Academy of Sciences XDB42020301 (to C.-Z.L.), and NSF grants 2114652 and 1657983 (to H.J.B.D.). **Author contributions:** Sample collection: H.J.B.D. Measurement: Z.-Y.Z. and W.W. Numerical modeling: J.-F.Y. and Y.L. Interpretation: All authors. Writing—original draft: C.-Z.L. Writing—review and editing: C.-Z.L., R.N.M., H.J.B.D., and A.W.H. **Competing interests:** The authors declare that they have no competing interests. **Data and materials availability:** All data needed to evaluate the conclusions in the paper are present in the paper and/or the Supplementary Materials. The numerical code I2VIS used for numerical modeling (developed by T. Gerya) is freely available at https://doi.org/10.17605/OSF.IO/bnvth.

Submitted 12 December 2021
Accepted 15 April 2022
Published 1 June 2022
10.1126/sciadv.abn6749

ScienceAdvances

Archean cratonic mantle recycled at a mid-ocean ridge

Chuan-Zhou LiuHenry J.B. DickRoss N. MitchellWu WeiZhen-Yu ZhangAlbrecht W. HofmannJian-Feng YangYang Li

Sci. Adv., 8 (22), eabn6749. • DOI: 10.1126/sciadv.abn6749

Science Advances (ISSN) is published by the American Association for the Advancement of Science. 1200 New York Avenue NW, Washington, DC 20005. The title *Science Advances* is a registered trademark of AAAS.